

AD-A037 555

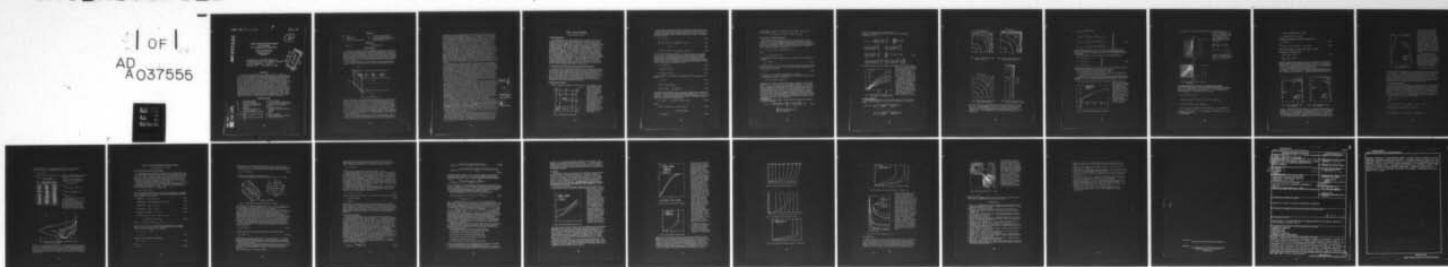
POLYTECHNIC INST OF NEW YORK FARMINGDALE AERODYNAMIC--ETC F/G 20/4  
LAMINAR FLOW IN RECTANGULAR CHANNELS. PART I: ENTRY ANALYSIS. P--ETC(U)  
DEC 76 S G RUBIN, P K KHOSLA, S SAARI AF-AFOSR-2635-74

UNCLASSIFIED

AFOSR-TR-77-0193

NL

1 OF 1  
AD  
A037555



END

DATE  
FILMED  
4-77

ADA037555

2

## LAMINAR FLOW IN RECTANGULAR CHANNELS

Part I: Entry Analysis

Part II: Numerical Solution for a Square Channel

S. G. Rubin, P. K. Khosla and S. Saari

Polytechnic Institute of New York  
Aerodynamic Laboratories  
Farmingdale, N.Y.

Proceedings of the ASME Symposium  
on Numerical/Laboratory Computer Methods  
in Fluid Mechanics pp29-51  
December 1976 published by ASME

ABSTRACT

Laminar incompressible flow in rectangular channels is considered. In Part I, the entry region is evaluated by a boundary layer/potential core analysis. It is shown that the three-dimensional displacement induced potential flow can be described with a pair of two-dimensional potential functions. Second-order boundary layer solutions, with and without surface mass transfer, are determined; an interesting secondary flow reversal is predicted. In Part II, numerical solutions are obtained for the viscous channel equations, which are derived from the asymptotic theory of Part I. A two stream function, velocity, vorticity system, independent of the Reynolds number, is solved with a combined iterative ADI/point-relaxation numerical procedure. A single calculation applies for all Reynolds numbers, which appears only in the coordinate scaling. The axial flow behavior of Parts I and II are in good agreement in the asymptotic entry region where both analyses apply. Secondary flow reversal is calculated; however, the grid is too crude for quantitative comparisons. Numerical solutions are obtained until fully developed conditions are achieved. Agreement with experimental data is good.

NOMENCLATURE

a	= channel half height	$\beta$	= constant 1.21678
b	= channel half width	$\epsilon$	= 1 for rectangular channel and zero for two-dimensional channel
f	= defined by equation (I. 4a)	$\eta$	= boundary layer coordinate
m	= parameter defining mass transfer	$\lambda$	= b/a
p	= pressure	$\nu$	= kinematic viscosity
Re	= Reynolds number based on channel half width	$\xi$	= normalized distance along the channel
u, v, w	= velocities along the coordinate axes	$\rho$	= density
U, V, W	= induced velocities in inviscid flow	$\sigma$	= a/b
x, y, z	= distance along the coordinate axes	$\phi$	= velocity potential
		$\psi$	= stream function for cross flow
		$\Omega$	= stream wise vorticity

DDC FILE COPY

### Subscripts

ent = entry	n = surface normal direction
0 = zeroth order	m = represents mass transfer
1 = 1st order	i, j, k = characterize the finite-difference grid at the point $\xi, y, z$
e = edge of the boundary layer	

### Superscript

* = iteration	~ = normalized value
---------------	----------------------

## INTRODUCTION

Laminar incompressible flows in straight two-dimensional, axisymmetric and rectangular channels have been previously investigated by a variety of analytic and numerical techniques. These are typified by the linear boundary layer (Oseen) approximation [1] for evaluating the axial velocity and pressure history downstream of an initial entry region, more exact numerical analyses using the boundary layer [2, 3] or Navier-Stokes equations [4-6], and finally a boundary layer/potential core expansion method [7-9] that models the flow in the entry region.

From these investigations, the internal flow in a three-dimensional rectangular channel can be portrayed by the various regions depicted in Fig. 1.

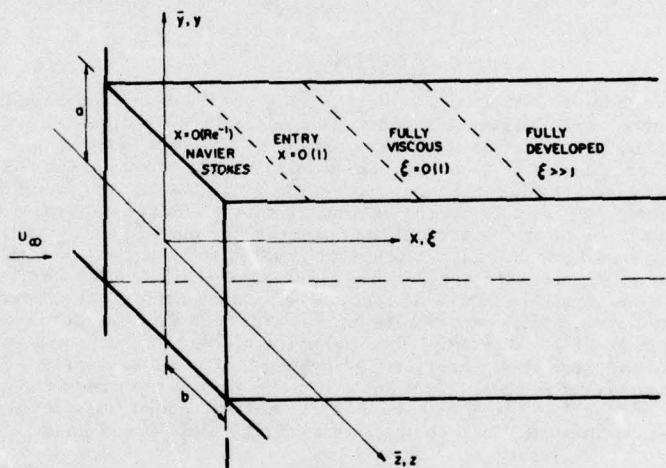


Fig. 1 Channel geometry

At the leading edge, a small Navier-Stokes entrance region, where  $x = O(R_e^{-1})$ , develops.  $R_e = U_\infty a / \nu$  is the Reynolds number based on the channel half-height  $a$ , the kinematic viscosity  $\nu$ , and the undisturbed stream  $U_\infty$ . The axial distance  $x$  is normalized with  $a$ . Complete Navier-Stokes solutions are required in order to describe this entrance flow. However, for large values of  $R_e$ , this length is so small that extraordinary axial grid resolution is required; moreover, the surface viscous layers are so thin that an extremely fine mesh is also necessary normal to the channel walls. For these reasons, an accurate description of this leading edge flow is quite difficult to obtain. Satisfactory solutions are not currently available, and this flow will not be considered here.

Following the Navier-Stokes region is the so-called entry flow, where  $x = O(1)$ . For this region, the axial gradients in the surface viscous layers have diminished, and therefore boundary layer theory is now applicable. As



the boundary layers grow downstream, the potential core will be appreciably affected by the viscous displacement effects. A systematic matched viscous/inviscid expansion procedure is required. This analysis has been completed for two-dimensional cascades [7] and inlets [8,9]. Agreement with solutions of the complete Navier-Stokes equations [5] is quite good, so that the validity of the boundary layer procedure has been established. In the downstream asymptotic portion of the entry flow, where  $x \gg 1$ , the solutions assume a particularly simple form in terms of the coordinate  $\xi = (2x/R)^{1/2}$ . The constant  $\beta = 1.21678$ , and  $\xi$  is small but finite; e.g.,  $\xi < 0.2$ . Therefore, for large  $R$  the entry flow can extend many channel widths downstream. In this asymptotic entry region the axial velocity is uniform across the potential core and the effects of different initial conditions are no longer discernible [7-9].

Further downstream the surface boundary layers become so thick that they fill a significant portion of the channel. The boundary layer/inviscid core expansion procedure is no longer convergent and a fully viscous channel flow must now be considered. In this flow domain  $\xi = O(1)$  and the axial flow gradients are small, but finite, throughout the channel. Boundary layer-like equations govern this flow regime. Numerical solutions are required. Finally, for  $\xi = \xi_{ent} \gg 1$ , the axial gradients vanish entirely and fully developed conditions are achieved. The distance  $\xi_{ent}$  has been termed the channel "entrance length".

In the present analysis all flow regimes downstream of the leading edge Navier-Stokes flow are considered for rectangular inlets. The paper is given in two parts. In Part I the entry region is considered with a matched boundary layer/potential core procedure similar to that used in two dimensions. This analysis applies for a three-dimensional cascade or what is more appropriately termed a baffle configuration. The solutions for the asymptotic entry flow, where the effects of the external geometry vanish, [9] are obtained by transform methods. As in two dimensions a uniform axial flow is found in the potential core region. Second-order boundary layer solutions, with and without surface mass transfer, are obtained for both the axial and secondary flows. A simplified result is found for the secondary flow behavior in the potential core; in the boundary layers, the secondary flow closely resembles that found along an infinite axial corner intersection. [10,11]

In Part II, numerical solutions are obtained for a square inlet, although the analysis is developed for a rectangular channel. These results can be considered to apply from the asymptotic entry region to the fully developed region. Comparisons with the analytic solutions for the asymptotic entry flow, where the analyses of Parts I and II overlap, are possible. Of particular interest in this investigation is the evaluation of the axial shear stress and the accurate resolution of the secondary flow behavior. Previous numerical studies [2-4] of this geometry have concentrated on the axial velocity and pressure distributions. One of the conclusions of the present investigation is that this axial flow behavior is virtually insensitive to the treatment of the secondary flow, although the inverse is not true. In the present study, converged secondary flow solutions are obtained, and within the limitation of the relatively coarse grids considered here the solutions appear to be quite reasonable.

It is shown that a system of boundary layer equations describe the entire channel flow downstream of the entry region, where  $\xi = O(1)$ . With an appropriate transformation of the axial coordinate from  $x$  to  $\xi$  the Reynolds number  $R$  can be scaled out of the equations. Reynolds number dependence appears only when the physical axial location  $x$  is specified. A system of equations including the axial velocity, axial vorticity and a pair of stream functions for the rotational secondary motion is developed. The axial pressure variation or surface shear stress is fixed by mass conservation. A predictor-corrector method is used for the axial velocity and vorticity, and a point relaxation procedure is used for the secondary motion.

Complete numerical solutions with and without secondary motion have been obtained. Near the entrance a small overlap region where both the analytic entry solution and downstream numerical solution apply is discerned. The agreement is quite reasonable, even though only a few grid points lie within the very thin boundary layers. The numerical solutions for the secondary motion exhibit a reversed profile predicted by the entry solutions of Part I.

ACCESSION for	
IS	White
NO	Buff
CLASSIFIED	
IDENTIFICATION	
BY	
DISTRIBUTION/AVAILABLE	
Dist.	AVAIL. and
A	



## PART I - ENTRY ANALYSIS

S. G. Rubin and S. Saari

### 1.1 Flow Description

The flow behavior in the entry region of Fig. 1, where  $x = O(1)$ , is considered. The entry flow is characterized by the formation of thin surface viscous layers with a large central inviscid core. A viscous/inviscid expansion procedure is applicable. For the entry analysis, rectangular channels formed by a doubly infinite baffle configuration is assumed. A uniform irrotational upstream flow is also specified. In reference [12] rotational entry is also considered. The symmetry inherent in this baffle geometry greatly simplifies the evaluation of the displacement induced core flow. The entry analysis for a single inlet is very complex. For two dimensions this geometry has been evaluated by a Weiner-Hopf technique [9]; it has been shown that in the asymptotic entry flow, for  $x \gg 1$  or  $\xi = O(1)$ , the effects of the entrance geometry are no longer important. Therefore, the cascade and single inlet solutions agree in this region. For the rectangular channels considered here, the asymptotic entry behavior in the core region is determined by a Fourier transform solution for  $x \gg 1$ . The entry flow for  $x = O(1)$  is determined by the method of images. In both cases the three-dimensional rectangular channel solution can be represented by a pair of locally two-dimensional solutions previously determined in reference [7].

### 1.2 Viscous/Inviscid Expansion Analysis-Potential Core Solution

In the entry region the large axial gradients, important in the leading edge Navier-Stokes flow, are small when compared with the surface normal variations and therefore boundary layer theory is applicable. This behavior has previously been observed in the entry region of two-dimensional channels, [7-9]; further confirmation for the asymptotic entry region of two-dimensional inlets, where higher-order terms in the boundary layer expansion are required, is given in section 1.3 of the present paper. In this section, the leading terms describing the boundary layer and potential core behavior are obtained for the entry and asymptotic entry flows.

#### Boundary Layer Analysis

The flow in the entry region is depicted in Fig. 2.

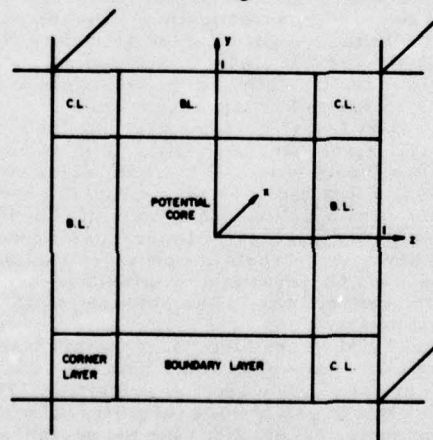


Fig. 2 Description of entry flow

Thin boundary layers grow along the walls and an inviscid core region is located centrally in the channel. At the corners the interfering boundary layers lead to a boundary region termed the corner layer. This flow has been studied extensively for an infinite corner, see references [10, 11], and can be neglected to lowest-order in the boundary layer analysis. We will return to the corner flow later in this section.

Since the flow gradients are large only in the surface normal direction, the standard boundary layer equations are obtained on each wall. For the remainder of the boundary layer analysis in this paper, the wall  $\bar{y} = -a$  will be considered. Similar results are obtained for the other walls. The boundary layer equations are

$$u_x + \tilde{v}_y + \sigma \tilde{w}_z = 0 \quad , \quad (I.1a)$$

$$u u_x + \tilde{v} u_y + \sigma \tilde{w} u_z = -p_x + \frac{1}{R_e} (u_{yy} + \sigma^2 u_{zz}) \quad , \quad (I.1b)$$

$$p_y = 0 \quad , \quad (I.1c)$$

$$u \tilde{w}_x + \tilde{v} \tilde{w}_y + \sigma \tilde{w} \tilde{w}_z = -\sigma p_z + \frac{1}{R_e} (\tilde{w}_{yy} + \sigma^2 \tilde{w}_{zz}) \quad , \quad (I.1d)$$

where  $u, \tilde{v}, \tilde{w}$  are normalized with  $U_\infty$ ;  $x, y$  with  $a$ ;  $z$  with  $b$  and  $p$  with  $\rho U_\infty^2$ ;  $\sigma = a/b = \lambda^{-1}$ . The diffusion terms in the axial direction are neglected as they are  $O(R_e^{-1})$  smaller than the surface normal ( $y$ ) variations. In the boundary layer, cross derivatives ( $z$ ) are also small when compared with normal changes, but are important in the corner layers and may be required for the second-order boundary layer analysis of the following section. Using standard boundary layer assumptions, we have

$$u = u_0 + R_e^{-\frac{1}{2}} u_1 + \dots \quad , \quad (I.2a)$$

$$\tilde{v} = R_e^{-\frac{1}{2}} \tilde{v}_1 + R_e^{-1} \tilde{v}_2 + \dots \quad , \quad (I.2b)$$

$$\tilde{w} = R_e^{-\frac{1}{2}} \tilde{w}_1 + R_e^{-1} \tilde{w}_2 + \dots \quad , \quad (I.2c)$$

where  $y = O(R_e^{-\frac{1}{2}})$ ;  $x, z = O(1)$ . To lowest order in  $R_e^{-\frac{1}{2}}$ , equations (I.1) become

$$u_{0x} + \tilde{v}_{1y} = 0 \quad , \quad (I.3a)$$

$$u_0 u_{0x} + \tilde{v}_1 u_{0y} = \frac{1}{R_e} u_{0yy} \quad , \quad (I.3b)$$

$$u_0 \tilde{w}_{1x} + \tilde{v}_1 \tilde{w}_{1y} = -\sigma p_{1z} + \frac{1}{R_e} \tilde{w}_{1yy} \quad , \quad (I.3c)$$

The axial pressure gradient is zero, since the inviscid stream is undisturbed and uniform. Equations (I.3) with the boundary conditions  $u = \tilde{v} = 0$  at  $y = -1$ , and  $u \rightarrow U_\infty$  for  $y \rightarrow y_e$  are precisely those of the flat plate boundary layer. The subscript  $e$  denotes the edge of the boundary layer. The solution of these equations is well-known [13] and given by

$$u_0 = f_0'(\eta) \quad , \quad \tilde{v}_1 = (2xR_e)^{-\frac{1}{2}} (\eta f_0'(\eta) - f_0(\eta)) \quad , \quad (I.4a)$$

where

$$f_0''(\eta) + f_0(\eta) f_0'(\eta) = 0 \quad , \quad f_0(0) = f_0'(0) = 0 \quad , \quad (I.4b)$$

$$f_0''(0) = 0.469600 \quad .$$

$$\eta = yR_e^{\frac{1}{2}} (2x)^{-\frac{1}{2}} \quad . \quad (I.4c)$$

Introducing the notation  $\xi^2 = \beta^2 2x/R_e$ , we have  $\eta = \frac{y\beta}{\xi}$ . For  $y \rightarrow y_e$  or  $\eta \rightarrow \infty$ , we find  $\tilde{v}_1 \rightarrow \beta (2xR_e)^{-\frac{1}{2}} = \beta^2 \xi^{-1} R_e^{-1}$ , where  $\beta = 1.21678$ .

#### Potential Core: Displacement Effects

The surface boundary layers perturb the central inviscid core. The effective core area is diminished thereby accelerating the flow. Since the inviscid flow is irrotational the three-dimensional Laplace equation must be solved for the perturbed core flow. Capital letters are used here to distinguish the potential flow variables from those of the boundary layer. A unified notation is used in the figures. Therefore,

$$\varphi = U_\infty \left[ x + R_e^{-\frac{1}{2}} \varphi_1(x, y, z) \right], \text{ and } \nabla^2 \varphi_1 = 0.$$

Also,

$$U = \varphi_x = U_\infty + R_e^{-\frac{1}{2}} U_1, \text{ etc.}$$

By matching with the inner boundary layers, we obtain for  $x > 0$  the boundary conditions

$$\varphi_{1n} = \beta (2x)^{-\frac{1}{2}} \quad (\text{I. 5a})$$

on all walls, where  $n$  denotes the surface normal direction measured positive inward; e.g. on  $y=1$ ,  $n=-y$ , etc. For  $x < 0$ , with the baffle configuration, the symmetry conditions lead to

$$\varphi_{1n} = 0 \quad (\text{I. 5b})$$

Finally, for  $x \rightarrow -\infty$  we require the uniform flow condition,  $\varphi_1 = 0$ .

In view of the symmetry, and the fact that the boundary  $\varphi_1$  conditions (I. 5) are independent of  $y$  and  $z$ , we can write

$$\varphi_1(x, y, z) = \varphi_1^1(x, y) + \varphi_1^2(x, z),$$

where  $\varphi_1^1$  and  $\varphi_1^2$  satisfy two-dimensional Laplace equations. The boundary conditions on  $y = \pm 1$  apply to  $\varphi_1^1$ , since  $\varphi_{1y} = 0$ , and those on  $z = \pm 1$  apply to  $\varphi_1^2$ . Therefore the three-dimensional Laplace equation and associated boundary conditions are satisfied by a pair of two-dimensional solutions each corresponding to the entry solution in a two-dimensional cascade. This is a significant simplification, since the two-dimensional solutions are given in Van Dyke [7] by the method of images and by Fourier transform techniques. The complete three-dimensional analysis and details of the solution are given in reference [12]. The image technique is preferable for the entry flow, while the transform procedure is preferable in the asymptotic entry region. The analysis and solutions are summarized below:

#### Image Solution

With the appropriate image or Green's function distributions, we obtain the following solutions:

$$\begin{aligned} \tilde{v}_1 = \varphi_{1y} = \frac{\beta}{2} & \left\{ \left( \frac{(x^2 + y^2)^{\frac{1}{2}} + x}{x^2 + y^2} \right)^{\frac{1}{2}} + \sum_{n=1}^{\infty} \left( \frac{(x^2 + (2n+y)^2)^{\frac{1}{2}} + x}{x^2 + (2n+y)^2} \right)^{\frac{1}{2}} \right. \\ & \left. - \sum_{n=1}^{\infty} \left( \frac{(x^2 + (2n-y)^2)^{\frac{1}{2}} + x}{x^2 + (2n-y)^2} \right)^{\frac{1}{2}} \right\}. \end{aligned} \quad (\text{I. 6a})$$



Note that  $\varphi_1^2$  does not appear in this expression.  
 $\tilde{W}_1 = \varphi_1$  is obtained from (I. 6a) with  $y \sim \sigma z$  and  $n \sim \sigma n$  inside the summation  $n = 1$  to  $\infty$ .

$$\begin{aligned}
 U_1 = \varphi_{1x} = & -\frac{\beta}{2} \left\{ \left( \frac{(x^2 + y^2)^{\frac{1}{2}} - x}{x^2 + y^2} \right)^{\frac{1}{2}} + \sum_{n=1}^{\infty} 2^{\frac{3}{2}} \left( (n-1)^{\frac{1}{2}} - n^{\frac{1}{2}} \right) \right. \\
 & + \left. \left( \frac{(x^2 + (2n-y)^2)^{\frac{1}{2}} - x}{x^2 + (2n-y)^2} \right)^{\frac{1}{2}} + \left( \frac{(x^2 + (2n+y)^2)^{\frac{1}{2}} - x}{x^2 + (2n+y)^2} \right)^{\frac{1}{2}} \right\} \\
 & - \left( \frac{(x^2 + \sigma^2 z^2)^{\frac{1}{2}} - x}{x^2 + \sigma^2 z^2} \right)^{\frac{1}{2}} + \sum_{m=1}^{\infty} 2^{\frac{3}{2}} \sigma^{-\frac{1}{2}} \left( (m-1)^{\frac{1}{2}} - m^{\frac{1}{2}} \right) \\
 & + \left( \frac{(x^2 + (2m-z)^2 \sigma^2)^{\frac{1}{2}} - x}{x^2 + \sigma^2 (2m-z)^2} \right)^{\frac{1}{2}} + \left( \frac{(x^2 + \sigma^2 (2m+z)^2)^{\frac{1}{2}} - x}{x^2 + \sigma^2 (2m+z)^2} \right)^{\frac{1}{2}} \Bigg\} \dots
 \end{aligned} \quad (I. 6b)$$

The centerline axial velocity for different rectangular inlets is shown in Fig. 3 for  $R_0 = 75$ . Typical solutions for the streamwise isovels at various locations in the entry flow are shown on Fig. 4 for different rectangular inlets. It is interesting to note that for very small values of  $x$  the behavior is monotonic. For larger  $x$  values a valley in the axial flow distribution is predicted. This behavior has been observed in two-dimensional Navier-Stokes solutions [4-6]. Finally, for even larger  $x$  values the behavior is once again monotonic, but the direction of increasing  $u$  has changed from that found for small  $x$ . A typical solution for a 5xl channel is shown on Fig. 4d.

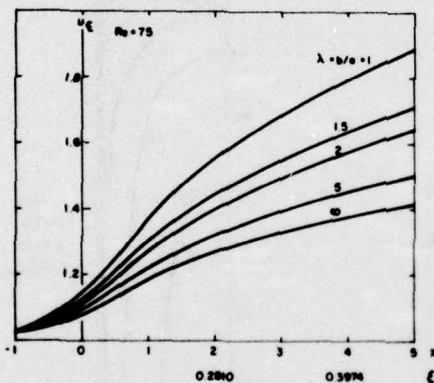


Fig. 3 Axial velocity distribution in entry region - rectangular channel

#### Transform Solutions

If the potential problem is solved by Fourier transforms, the same pairwise two-dimensional behavior occurs and the solution for  $\varphi_1$  is as follows [7,12]:

$$\begin{aligned}
 \varphi_1(x, y, z) = & \frac{-\beta}{4\pi^{\frac{1}{2}}} \int_{-\infty}^{\infty} \frac{(1 + i \operatorname{sgn} s) e^{-isx} \cosh s(1-y)}{s |s|^{\frac{1}{2}} \sinh s} ds \\
 & - \frac{\beta}{4\pi^{\frac{1}{2}}} \int_{-\infty}^{\infty} \frac{(1 + i \operatorname{sgn} s) e^{-isx} \cosh \sigma s(1-z)}{s |s|^{\frac{1}{2}} \sinh \sigma s} ds
 \end{aligned} \quad (I. 7)$$

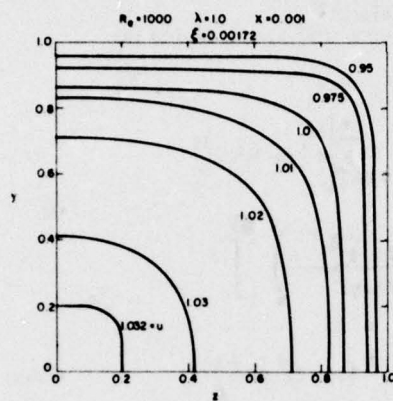


Fig. 4a Streamwise isovels at inlet-square channel

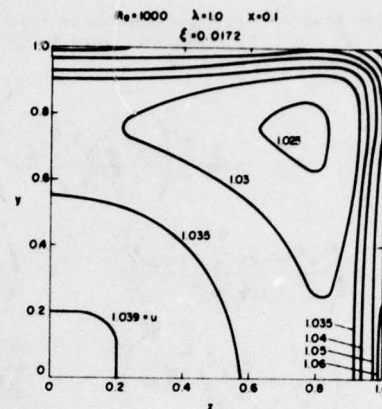


Fig. 4b Streamwise isovels in entry region-square channel

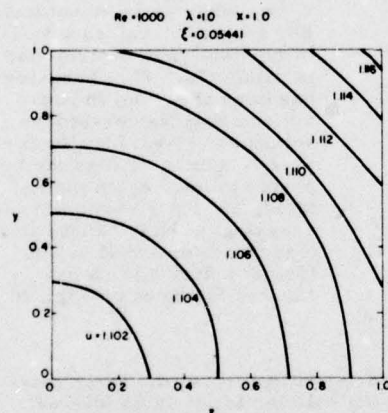


Fig. 4c Streamwise isovels in entry region-square channel

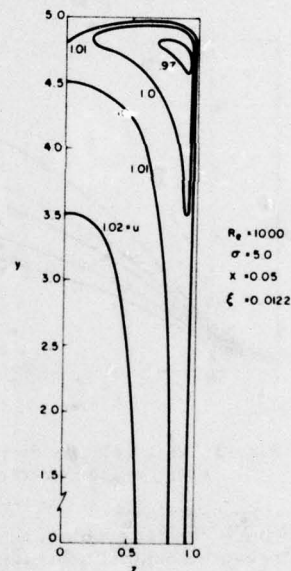


Fig. 4d Streamwise isovels near entry-rectangular channel

The velocities  $\varphi_{1x}$  etc. are difficult to evaluate for general values of  $x$ , but for  $x \gg 1$  (the asymptotic entry flow) it is possible to obtain asymptotic expressions using the generalized Fourier transform concept outlined by Lighthill [14]. More complete details of this procedure can be found in references [7,12]. The results, for  $x \gg 1$ , lead to the following expansions of solution (I. 7).

$$\left. \begin{aligned}
 U_1 = \varphi_1_x &= 2^{\frac{1}{2}} \theta \left[ x^{\frac{1}{2}} (1 + \sigma) + \right. \\
 &\quad \left. \frac{1}{24} x^{-3/2} (3y^2 - 1) + \sigma^3 \theta (3z^2 - 1) \right] + \dots \\
 V_1 = \varphi_1_y &= -2^{-\frac{1}{2}} \theta y \left[ x^{-\frac{1}{2}} + (1-y^2)/8x^{5/2} \right] + \dots \\
 W_1 = \varphi_1_z &= -2^{-\frac{1}{2}} \theta z \left[ x^{-\frac{1}{2}} + \sigma^2 (1-z^2)/8x^{5/2} \right] + \dots
 \end{aligned} \right\} \quad (I. 8a)$$

The non-monotonic behavior seen earlier in the series solutions is still apparent in the asymptotic solution. In reference [12] the asymptotic and series behavior for  $x < 0$  is presented. Here we are concerned only with the internal flow.

For very large  $x \gg 1$ , the full solutions for the velocities become

$$\left. \begin{aligned}
 U &\sim 1 + (1 + \sigma) \xi + \dots \\
 V &\sim -\sigma^2 \xi^{-1} R_e^{-1} y + \dots \\
 W &\sim -\sigma^2 \xi^{-1} R_e^{-1} z + \dots
 \end{aligned} \right\} \quad (I. 8b)$$

Therefore the asymptotic entry flow and onset of the fully viscous channel flow have the following properties in the central core region:

- (1) The axial velocity is uniform across the channel.
- (2) The relevant axial flow coordinate is  $\xi = O(1)$
- (3) The secondary velocities are  $O(R_e^{-1})$  and not  $O(R_e^{-\frac{1}{2}})$  as in the entry flow boundary layers and potential core.

This behavior has previously been found for two-dimensional channels and corresponds to the form originally assumed by Schlichting [13] in his expansion technique. For two-dimensional channels  $\bar{V}$  is given by (I. 8b),  $W = 0$  and  $U \sim 1 + \xi$ .

Fig. 5 depicts the axial flow variation along the channel centerline as

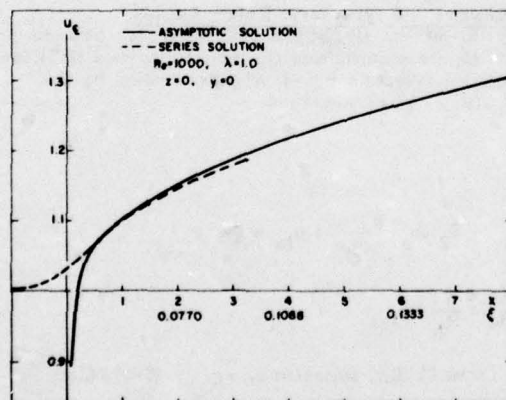


Fig. 5 Entry flow solutions- Square channel

obtained by the image and asymptotic solutions. It is interesting that the asymptotic form is achieved for relatively small values of  $x$ , even though it has been derived for  $x \gg 1$ . Similar behavior is found at other channel locations. This allows for the use of the simplified formulas (I. 8b) over a significant portion of the entry region.



Finally, Fig. 6 depicts the qualitative behavior of the secondary flow

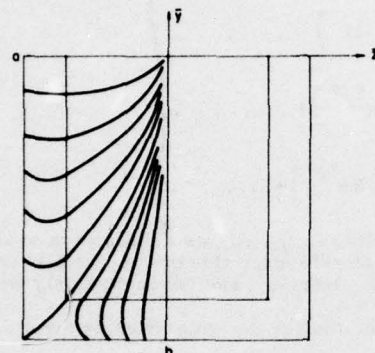
stream lines projected onto the  $(y, z)$  cross plane. For a square channel these lines are straight, for a  $2 \times 1$  channel parabolic, and in general they are given by the equation:

$$\frac{d\bar{y}}{dz} = \frac{V}{W_1} = \frac{y}{z} = \frac{1}{\sigma} \frac{\bar{y}}{z},$$

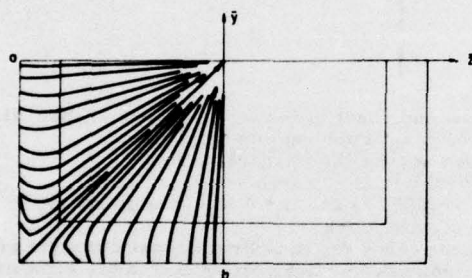
$$\bar{z} = c\bar{y}^\sigma \quad \text{or} \quad z = c\sigma y^\sigma,$$

(I. 8c)

where  $c$  is a different constant for each of the streamlines. For a square channel  $z = cy$ ; for  $\sigma = 2$ ,  $z = 2cy^2$ , etc.



(i)  $\sigma = 2$



(ii)  $\sigma = 1$

Fig. 6 Asymptotic flow projection on cross plane.

### I. 3. Second-Order Boundary Layers - Asymptotic Entry Region

With the asymptotic potential solutions (I. 8b) the second-order boundary layers can now be evaluated. With the expansions (I. 2) in equations (I. 1), the axial and secondary motion along the surface  $y = -1$  are described by the following equations. Terms of  $O(R_e^{-3/2})$  are retained.

$$u_{1x} + R_e^{-1/2} \tilde{v}_{2y} + \sigma w_{1z} = 0,$$

$$u_0 u_{1x} + u_1 u_{0x} + R_e^{-1/2} \tilde{v}_1 u_{1y} + \tilde{v}_2 R_e^{-1/2} u_{0y} + p_{1x} = \frac{1}{R_e} u_{1yy},$$

$$u_0 \tilde{w}_{1x} + R_e^{-1/2} \tilde{v}_1 \tilde{w}_{1y} = -\sigma p_{1z} + \frac{1}{R_e} \tilde{w}_{1yy}.$$

As  $y = y_e$ ,  $u_1 = U_1$ ,  $\tilde{w}_1 = \tilde{W}_1$  from (I. 8b); therefore,  $-p_{1x} = (1+\sigma) \delta(2x)^{-1/2}$ , and  $-\sigma p_{1z} = \epsilon 2^{-3/2} \delta z x^{-3/2}$ ;  $\epsilon = 1$  for rectangular channels and  $\sigma = \epsilon = 0$  for two-dimensional channels.

Assuming that

$$u = f'_0(\eta) + (1+\sigma) \xi f'_1(\eta) = u_0 + R e^{-\frac{1}{2}} u_1 \quad ,$$

$$\tilde{w}_1 = -\epsilon \beta z(2x)^{-\frac{1}{2}} h'(\eta) = \tilde{w}_1 h'(\eta) \quad ,$$

the following equations are obtained for  $f_1(\eta)$  and  $h(\eta)$  :

$$h''' + (f_0 h')' = 1 \quad , \quad (I. 9a)$$

$$\text{and} \quad f_1''' + f_0 f_1'' - f_0' f_1' + 2f_0'' f_1 = -1 + \epsilon f_0'' h / (1+\sigma) \quad , \quad (I. 9b)$$

$$\text{where from continuity } \tilde{v}_2 = \beta \left[ (1+\sigma) (\eta f_1' - 2f_1(\eta)) + \epsilon h(\eta) \right] \quad .$$

The boundary conditions become

$$f_1(0) = f_1'(0) = h'(0) = 0 \quad , \quad (I. 9c)$$

$$\lim_{\eta \rightarrow \infty} f_1'(\eta) = h'(\eta) = 1$$

Equation (I. 9b) for the secondary velocity  $\tilde{w}_1$  is identical with that derived in earlier studies of the flow along an unbounded corner [10]. An interesting secondary flow reversal is predicted, and this behavior is shown qualitatively on Fig. 6. The core solution was discussed in section I. 2. The reversed flow profile is depicted more accurately in section I. 4.

The second-order axial flow is described by equation (I. 9a). For two-dimensions ( $\epsilon = 0$ ) this equation was considered by Schlichting [13] and Wilson [8]. Solutions are shown on Fig. 7. Also presented is the potential core

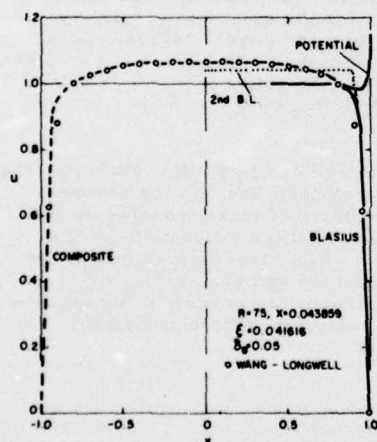


Fig. 7a Two-dimensional entry flow solutions

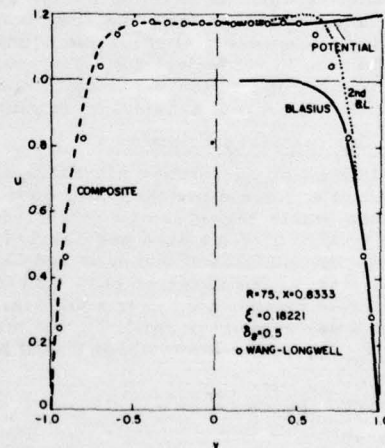


Fig. 7b Two-dimensional entry flow solutions

behavior, the first-order Blasius solution, and a composite viscous/inviscid profile. Comparisons are made with the Navier-Stokes solutions of Wang and Longwell [5]. The agreement is reasonably good for  $\xi < 0.2$  and therefore the applicability of the expansion procedure in the entry flow is confirmed. For three-dimensional flows, solutions have been obtained for a square inlet ( $\sigma = 1$ ). These results will be presented in Part II, where comparisons with

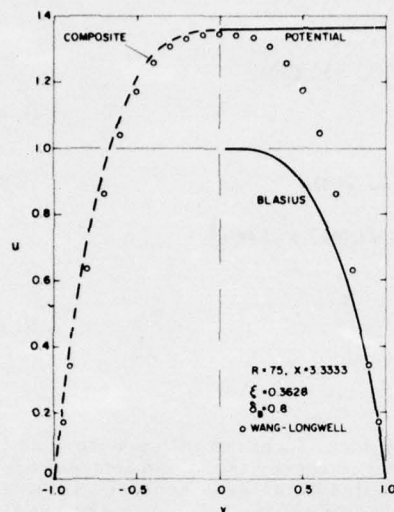


Fig. 7c Two-dimensional entry flow solutions.

the viscous channel solutions are included. The boundary layer-like behavior found in (I.8) is used to describe the downstream viscous channel flow. The expansion procedure shows evidence of divergence for values of  $\xi > 0.2$ . Higher-order terms (not shown) exhibit behavior typical of divergent asymptotic series. Also, eigenvalues of equation (I.9a) must then be included in the expansion. These introduce unknown constants which must be evaluated by other means, see references [8, 9].

A final comment on the secondary behavior in the entry region concerns the corner layers of Fig. 2. The corner flow for an infinite geometry has been presented in great detail in earlier studies [10, 11]. Significantly, for the channel the secondary flow behavior near the corners ( $z \rightarrow \pm 1$ ) gives

$$\tilde{w}_1 \sim \pm 8(2x)^{-\frac{1}{2}} R_e^{-\frac{1}{2}} h'(\eta).$$

This is precisely the result found for the unbounded corner flow and therefore, in the asymptotic entry region, the solutions of references [10, 11] apply to the channel as well. A swirling motion shown qualitatively on Fig. 6 is obtained.

This completes the entry flow description for the axial and secondary motion in the potential core, the boundary layers and corner layers. Comparisons with numerical solutions are given in Part II. In section I.4 a brief description of the flow behavior allowing for surface mass transfer is presented. The effect of injection is particularly interesting.

#### I.4 Surface Mass Transfer

In view of the relative simplicity of the asymptotic entry flow analysis, the effect of surface mass transfer, both suction and injection, on the secondary motion in this region is now evaluated. The effects of mass transfer on the streamwise profiles have previously been calculated for a flat plate by the similarity analysis of Emmons and Leigh [15]. The mass injection is of the type  $\tilde{v} \sim x^{\frac{1}{2}}$ , or in terms of  $\xi$  and the normalized velocity  $v = \xi R_e^{-\frac{1}{2}} \tilde{v}$ , we obtain  $v = \text{constant}$ . For a uniform outer stream, as occurs in the asymptotic entry region for small  $\xi$ , the modified boundary layer equation for  $u = f'_m(\eta)$  on the lower channel wall becomes

$$f'''_m + f_m f''_m = 0,$$

where

$$f_m(0) = m, f'_m(0) = 0, \lim_{\eta \rightarrow \infty} [f'_m(\eta) \rightarrow 1, f_m(\eta) \sim \eta - \beta_m].$$

The normalized surface velocity  $v$  is given as

$$v = \beta^{-1}_m$$

$m > 0$  for injection;  $m < 0$  for suction,  $\beta = \beta_0 = 1.21678$ .



The solutions for  $f_m$  are tabulated in reference [15]. The asymptotic boundary condition<sup>m</sup> on the displacement velocity  $v$  becomes

$$\lim_{\eta \rightarrow \infty} v \sim \beta_m / \beta$$

$\beta_m$  is tabulated for several values of  $m$  in Table I; also presented are values of the shear stress parameter  $f_m''(0)$ .

Table I: Shear stresses with mass transfer

$m$	$\beta_m = -h_m''(0)$	$f_m''(0)$
-0.707	3.8118	0.0502
-0.495	2.5913	0.1512
-0.353	2.0929	0.2326
-0.177	1.8108	0.3460
-0.0707	1.3665	0.4191
0.0	1.21678	0.4696
0.0707	1.0755	0.5214
0.177	0.8766	0.6012
0.353	0.5724	0.7394
0.495	0.3475	0.8538
0.707	0.0330	1.0308
0.778	-0.0670	1.0910
0.848	-0.1650	1.1518

The normalized secondary velocity  $w$  can be defined as

$$w = (\beta_m / \beta) h_m'(\eta)$$

where

$$h_m''' + f_m h_m'' + f_m' h_m' = 1$$

and

$$h_m'(0) = 0, \lim_{\eta \rightarrow \infty} h_m'(\eta) = 1$$

also

$$h_m''(0) = -\beta_m$$

The solutions for  $h_m'$  and  $f_m'$  are shown in Fig. 8.

Mass injection increases the secondary flow reversal as well as the streamwise surface shear stress. With large suction the secondary flow reversal can be eliminated. On Table I it is seen

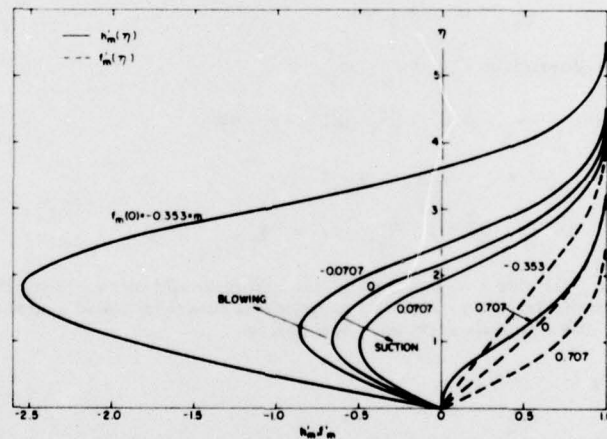


Fig. 8 Effects of mass injection on asymptotic velocity profiles in entry region.

that  $h_m''(0)$  changes sign at about  $m=0.71$ . The potential core solutions (I.8) for  $v$  and  $w$  are modified by the factor  $\beta_m / \beta$ , but the projected streamline pattern is unchanged. In the surface boundary layers the secondary motion is accentuated or reduced as depicted in Fig. 8. It is evident from the figure that the secondary flow patterns are significantly altered with even moderate mass transfer.

## Part II. - Numerical Solution For A Square Channel

S.G. Rubin and P. K. Khosla

### II.1 Flow Analysis - Fully Viscous Region

The boundary-layer/potential flow expansion procedure applicable in the entry region Fig. 1 and described in Part I fails in the downstream flow where  $x \gg 1$  or  $\xi = 0(1)$ . From the results of Part I we expect that the entry analysis (both series and asymptotic solutions) will apply many diameters downstream, e.g., for all  $\xi < 0.20$ ; but, for larger  $\xi$  values, the errors in the asymptotic boundary-layer/potential core expansion procedure increase as the boundary layers grow and begin to fill the channel.

From the results of Part I, it is seen that a fully viscous model is required. The equations are appropriately written in terms of the coordinates  $(\xi, y, z)$ . The normalized velocities are  $u = \bar{u}/U_\infty$ ,  $v = \xi R_e \beta^{-2} \bar{v}/U_\infty$ ,  $w = \xi R_e \beta^{-2} \bar{w}/U_\infty$ , and the normalized pressure is  $p = \bar{p}/\rho U_\infty^2$ , where

$$p = p_0 + R_e^{-1} p_1 + R_e^{-2} p_2$$

See Part I, equations I.8 for the asymptotic forms required here. Retaining only the lowest order terms in  $\xi R_e$  in each of the governing equations (see Part I, equations I.1), we obtain:

$$\text{Continuity: } u_\xi + v_y + \sigma w_z = 0 \quad (\text{II. 1})$$

$$\xi \text{ Momentum: } \xi \beta^{-2} \nabla^2 u = u u_\xi + v u_y + \sigma w u_z + p_{0\xi} \quad (\text{II. 2})$$

$$y \text{ Momentum: } p_{0y} = 0, \quad p_{1y} = 0 \quad (\text{II. 3})$$

$$z \text{ Momentum: } p_{0z} = 0, \quad p_{1z} = 0, \quad (\text{II. 4})$$

$$\text{Streamwise Vorticity: } \Omega = \sigma v_z - w_y, \quad (\text{II. 5})$$

$$\begin{aligned} \xi \beta^{-2} \nabla^2 \Omega = u \Omega_\xi + \tau v_\xi - \alpha w_\xi - \xi^{-1} (u \Omega + \tau v - \alpha w) \\ + v \Omega_y + \sigma w \Omega_z + \Omega (v_y + \sigma w_z) \end{aligned} \quad (\text{II. 6})$$

$$\text{where } \tau = \sigma u_z, \quad \alpha = u_y, \quad \nabla^2 = (\ )_{yy} + \sigma^2 (\ )_{zz},$$

and  $\sigma = a/b = \lambda^{-1} = 1$  for the square channel considered here. Equations (II.1, 6) are reformulated in terms of a potential function  $\varphi$  and a stream function  $\psi$  for the crossflow ( $v, w$ ). We define

$$\begin{aligned} v = \varphi_y + \sigma \psi_z \quad \text{and} \\ w = \sigma \varphi_z - \psi_y \end{aligned} \quad (\text{II. 7})$$

Therefore, (II.1, 5) become, respectively,

$$\nabla^2 \varphi = -u_\xi, \quad (\text{II. 8})$$

and

$$\nabla^2 \psi = \Omega. \quad (\text{II. 9})$$

Equations (II. 2, 6, 8, 9) describe the unknowns  $u, \Omega, \varphi, \psi$ .  $v$  and  $w$  are recovered from (II. 7). The streamwise pressure gradient  $p_z^*$  depends only on  $\xi$ , as seen from (II. 3, 4) and is specified by the mass conservation integral

$$\int_A u(\xi, y, z) dy dz = 1. \quad (\text{II. 10})$$

$A$  denotes the rectangular cross-sectional area.

The appropriate boundary conditions are shown on Fig. 9. It is easily

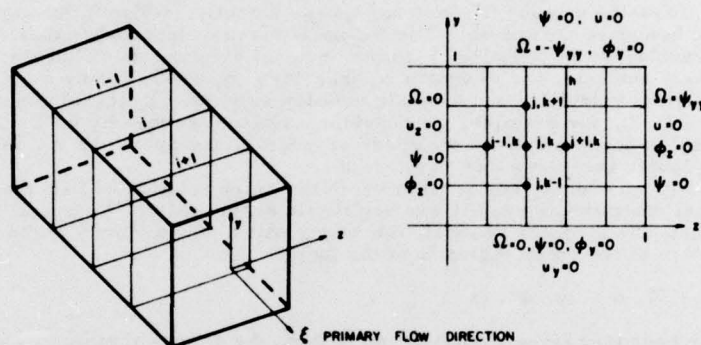


Fig. 9 Finite-difference grid and boundary conditions

proven that these conditions uniquely define  $\varphi$  and  $\psi$ . The zero normal mass flux condition on  $v$  and  $w$  is satisfied exactly. The no-slip conditions are satisfied indirectly through the surface vorticity relation.

For two-dimensional channels, solutions were also obtained with an alternate formulation in terms of the stream function and vorticity. The surface shear was determined with the mass conservation condition (II. 10). The pressure gradient  $p_x$  was then obtained by application of the momentum equation (II. 2) at the surface, where the no-slip conditions are applied. It is significant that fully converged solutions obtained at each streamwise location by the two procedures were identical. The accuracy of the final solution is therefore limited solely by the mesh size. A similar vorticity formulation is possible for three-dimensional flows, although it has not been used here.

Another important feature of the present formulation is the conservation implicit in the system (II. 8, 9). With the Neumann boundary conditions on  $\varphi$  it is necessary that

$$\int_A \nabla^2 \varphi dy dz = 0 \quad (\text{II. 11})$$

With the mass conservation condition (II. 10) we automatically satisfy

$$\int_A u_\xi dy dz = 0, \quad (\text{II. 12})$$

and therefore the integral condition (II. 11) is always satisfied. In an earlier study of this problem Briley [2] applied a similar procedure with a single potential function, but it was necessary to apply an iterative correction factor in order that (II. 11) be satisfied.

More important, however, the additional stream function provides a simple mechanism for exactly satisfying the vorticity ( $\Omega$ ) and secondary flow ( $v, w$ ) equations to any desired degree of accuracy. In this way we are able to

\* The zero subscript on  $p$  has been dropped.



rigorously examine the mutual interaction between the streamwise and secondary motions and thereby accurately evaluate the effect of one on the other. Finally, the asymmetry of  $\Omega$  leads to the additional condition

$$\iint_A \nabla^2 \psi \, dydz = 0.$$

This is insured by the boundary conditions relating  $\psi$  and  $\Omega$ .

The governing system for the downstream flow,  $\xi = 0(1)$ , and ultimately the fully developed region,  $\xi \gg 1$ , has now been described. It is significant that the Reynolds number  $R$  does not appear directly, either in the equations or in the boundary conditions. The Reynolds number dependence exists only in the transformation relating  $\xi$  to the physical distance  $x$ . Therefore, with the present analysis, the Reynolds number does not enter, in any way, into the numerical calculations. A single solution valid for all Reynolds numbers is obtained. If, for example, we consider a channel defined by  $0 < \xi < 1$ , then the Reynolds number defines the physical length of the duct. As  $R_e$  increases the duct length increases and vice-versa.

Finally, an overlap region where both the entry solution of Part I and the numerical downstream results are applicable should exist. We recall from Part I that, for a square channel, the asymptotic behavior found in the potential core of the entry region is of the form

$$u \sim 1 + 2\xi, \quad v \sim -y, \quad w \sim -z \quad (II.13)$$

while the boundary layer variation, away from the corner regions, is as follows:

$$\begin{aligned} u &\sim f'_0(\eta) + 2\xi f'_1(\eta) \\ w &\sim -zh'(\eta) \end{aligned} \quad (II.14)$$

These solutions approximate the viscous channel equations (II.1, 2, 6) for small values of  $\xi$ . Therefore, the numerical solutions for the downstream viscous channel flow, which are valid only for  $x \gg 1$ , should become meaningful for moderate values of  $\xi$ , where (II.13,14) are indicative of the flow behavior. The complete channel flow, away from the small leading edge Navier-Stokes region, is then described by the composite entry plus downstream solution.

## II.2 Numerical Methods

The governing equations (II.2, 6, 8, 9, 10) are solved numerically by a marching procedure starting at the leading edge  $\xi = 0$ . The initial conditions are assumed to be  $\Omega = v = w = 0$ . The axial velocity  $u$  is uniform and satisfies the mass conservation condition (II.10). At the walls the no-slip and zero mass transfer conditions are enforced. Since only the quarter channel is considered, symmetry conditions are prescribed along the center lines. The complete set of boundary conditions is shown on Fig. 9. These initial values are somewhat artificial and therefore the numerical solutions become meaningful only after the influence of the initial values become negligible, i.e., in the asymptotic entry flow described in Part I. In view of the parabolic character of the viscous channel equations, the only remaining influence of the initial values will be reflected in the mass conservation integral (10). This behavior has previously been verified for two-dimensional channels [4-6], where the asymptotic entry behavior is closely approximated by the numerical boundary layer solutions [7-9]. As will be shown in the present analysis, a similar overlap is found for a three-dimensional geometry.

Finite difference discretization is used for all derivatives. These are centered at the half point  $\xi_{i+\frac{1}{2}}$  in marching from  $\xi_i$  to  $\xi_{i+1}$ ; i.e., a Crank-Nicolson procedure. Therefore,

$$(u_\xi)_{i+\frac{1}{2}, j, k} = \frac{u_{i+1, j, k} - u_{i, j, k}}{\Delta \xi} \quad (II.15a)$$

$$(u_y)_{i+\frac{1}{2}, j, k} = \frac{u_{i, j+1, k} - u_{i, j-1, k} + u_{i+1, j+1, k} - u_{i+1, j-1, k}}{4h}, \quad (\text{II. 15b})$$

$$(u_{yy})_{i+\frac{1}{2}, j, k} = \frac{u_{i, j+1, k} - 2u_{i, j, k} + u_{i, j-1, k} + u_{i+1, j+1, k} - 2u_{i+1, j, k} + u_{i+1, j-1, k}}{2h^2} \quad (\text{II. 15c})$$

All other variables are discretized in a similar fashion; z derivatives are obtained from (II. 15) with  $j \rightarrow k$ ,  $k \rightarrow j$  and then transposing the subscripts. Non-linear terms such as  $uu_\xi$  in (II. 2) are treated with quasi-linearization, so that

$$(uu_\xi)_{i+\frac{1}{2}, j, k} = \frac{2u_{i+1, j, k}^* u_{i+1, j, k} - u_{i, j, k}^2 - u_{i+1, j, k}^{*2}}{2\Delta\xi},$$

where  $\Delta\xi$  denotes the step size and the asterisk superscript denotes the value, at the new location  $\xi_{i+1}$ , obtained from the previous iteration. The function  $u(\xi, y, z)$  is denoted by  $u_{i, j, k}$ , where  $\xi_i = (i-1)\Delta\xi$ ,  $y_j = (j-1)h$  and  $z_k = (k-1)h$ ;  $h$  is the uniform grid spacing in the  $(y, z)$  plane so that  $h=1/N$ .  $N$  is the number of grid intervals in the quarter channel, see Fig. 9.

For each equation (II. 2, 6, 8, 9) we obtain a system of the form

$$A_i u_{i+1, j+1, k} + B_i u_{i+1, j-1, k} + C_i u_{i+1, j, k} + D_i u_{i+1, j, k+1} + E_i u_{i+1, j, k-1} = F_i \quad (\text{II. 16})$$

$A_i, \dots, F_i$  depend only on the values at  $\xi_i$  or of the previous iteration (asterisks). The full equations are easily derived. Equation (II. 16) is solved with an ADI predictor-corrector method for  $u, \Omega$  and point SOR for  $\phi, \psi$ . For the former the tridiagonal matrices are inverted with the now standard two pass algorithm. In the ADI iterative procedure the  $u_{i+1, j+1, k}$  and  $u_{i+1, j-1, k}$  terms are treated implicitly in the predictor stage and the terms  $u_{i+1, j, k+1}$ ,  $u_{i+1, j, k}$  and  $u_{i+1, j, k-1}$  are implicit in the corrector stage. This procedure was found preferable to the line predictor-corrector method [16] as the symmetry properties of the flow variables were maintained to a high degree of accuracy. For the SOR calculations an optimum over-relaxation parameter  $\omega$  [17] for a square uniform grid with Dirichlet boundary conditions is specified;  $\omega \approx 2(1-\pi/(N+1))$ . This parameter also works quite well on the Neumann problem (II. 8) for  $\phi$ . For  $N=10$   $\omega \approx 1.43$ . For  $N=20$   $\omega \approx 1.72$ . For all equations, the system (II. 16) is diagonally dominant and appears to be stable even for relatively large values of  $\Delta\xi$ .

Finally, the pressure gradient in (II. 2) is updated by Newton extrapolation such that the mass flux condition is satisfied. The mass flux integral is approximated with the trapezoidal rule. The secondary velocities  $v$  and  $w$  are recovered from (II. 7).

The iterative procedure can be summarized as follows:

- (1) At station  $\xi_{i+1}$ , let  $p_\xi, \phi, \psi, \Omega$  assume their  $\xi_i$  values.
- (2) Calculate  $u_{i+1}$  from (II. 2) using iterative ADI.
- (3) Calculate  $\Omega_{i+1}$  from (II. 6) using iterative ADI.
- (4)  $\phi_{i+1}$  and  $\psi_{i+1}$  are found from (II. 8, 9) using SOR.
- (5) Update  $v_{i+1}$  and  $w_{i+1}$  from (II. 7).
- (6) Update  $(p_\xi)_{i+1}$  from (II. 10) and return to step (1).

At each  $\xi$  location this procedure continues until all values have converged to the specified tolerance, e.g. six decimal place accuracy.

In the vorticity streamfunction method discussed earlier, the evaluation of  $p_\xi$  in step (6) is replaced with the direct evaluation of the wall shear, e.g.

$\tau = u_y$  on  $y = -1$ , such that the mass flux condition (II.10) is satisfied. The pressure is then obtained by application of (II.2) at  $y = -1$ . The two procedures lead to identical results in two-dimensional channels. This latter approach would be preferred for problems in turbomachinery where local separation bubbles can be evaluated. This approach has previously been considered only for external flows [18].

### II.3 Results

The numerical solutions were obtained by considering the quarter channel with mesh widths  $h = 0.05$  (21 points) and  $h = 0.1$  (11 points), respectively. Therefore, in the entry flow where the boundary layers are very thin, the accuracy of the results near the channel walls is marginal. Further downstream, as the boundary layers thicken, the resolution increases markedly. All of the results are given as functions of the normalized axial length  $\xi$ , where we recall that  $\xi = 2xg^*/R_e$ . The solutions are independent of the Reynolds number, except for the normalization inherent in  $\xi, v, w$ . Note that for large  $R_e$  even relatively small values of  $\xi$  can correspond to axial distance of many channel widths.

The centerline velocity is depicted on Fig. 10a for the entry flow, and Fig. 10b shows the entire channel flow to fully developed conditions. Solutions

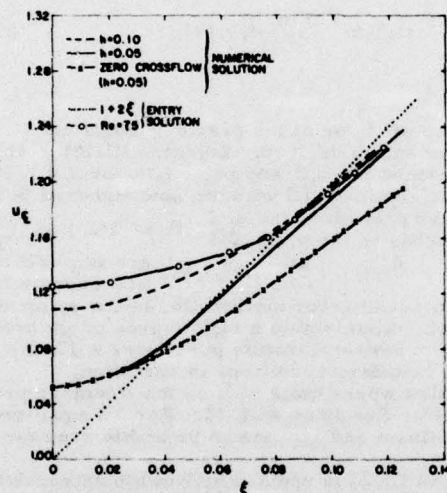


Fig. 10a Centerline velocity near inlet

with the coarse and fine grids are presented, as are solutions with zero crossflow (secondary flow). The different initial conditions with differing meshes result from the requirement that the mass flux conditions (II.10) be satisfied. Also shown are the entry solutions obtained in Part I. For a Reynolds number  $R_e = 75$  the series solutions are given; the  $R_e$  independent transform result ( $u \sim 1+2\xi$ ) describes the behavior of  $u$  in the asymptotic entry region. Finally, on Fig. 10b the experimental data of reference [19] are also included. For  $0.2 > \xi > 0.08$  the entry and numerical solutions with crossflow

are in good agreement with each other. The flow dependence on  $\xi$  and therefore independence of  $R_e$  is evident. The solutions with zero crossflow are somewhat lower than the other solutions, but are not significantly different. In fact, it can be concluded that the secondary motion has only a minor effect on the axial behavior. As seen on Fig. 10b, agreement with the data is good. Fully developed conditions are achieved for  $\xi = \xi_{ent} \approx 0.9-1.0$ . In previous studies, [1-6] the entrance length has been estimated to be in the range  $\xi_{ent} = 0.89-1.0$ . From Fig. 10b, it can be inferred that the entry region analysis is valid up to  $\xi = 0.2$ .

On Fig. 11 the axial velocity is compared with experimental data. Many additional comparisons were made, but since the agreement is similar to that of Fig. 11, and since the axial behavior has been described quite well in other investigations, these results are not included here. The axial velocity profiles along the centerline ( $z=0$ ) are shown on Fig. 12.



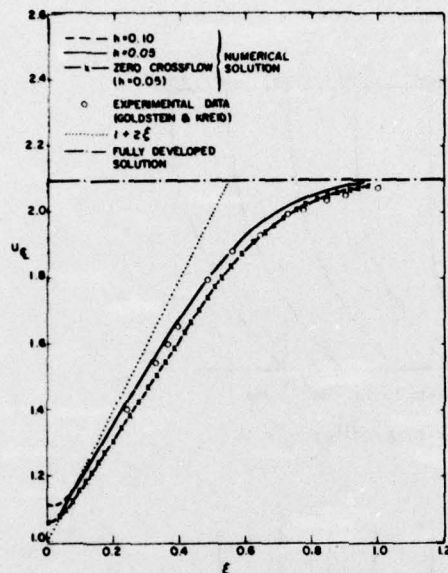


FIG. 10b CENTERLINE VELOCITY VARIATION

Fig. 10b Centerline velocity variation

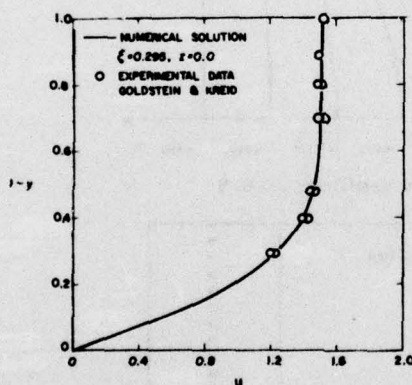


Fig. 11 Streamwise velocity profile

Blasius results and the second-order boundary layer solutions are in close agreement. As  $\xi$  increases the wall values ( $z=0.95$  or  $z=0.90$ ) decrease due to corner layer interference. As the boundary layers grow further, the mid-point values ( $z=0.5$ ) also fall below the centerline ( $z=0$ ) solutions. Second-order boundary layer theory is a significant improvement over the Blasius values in the entry flow ( $\xi < 0.2$ ); even for larger  $\xi$  values, where the theory is questionable, the results are within 20% of the numerical solutions. Once again, the solutions obtained by neglecting the secondary

Profiles for the secondary velocity near the corner region are given on Fig. 13. Reverse flow profiles have been calculated in the asymptotic entry region. Similar behavior was predicted by the entry analysis of Part I, section I.3. The decay of the secondary motion as fully developed flow conditions are attained is apparent. The resolution in the boundary layer region is insufficient to make quantitative comparisons of the numerical and entry analysis for the secondary motion. The flow reversal occurs over one-tenth of the channel cross-section or one-fifth of the total boundary layer thickness for  $\xi = 0.2$ . For the present calculations, this is at most two grid points. Even with the coarse mesh, the axial profiles (Fig. 14) agree quite well with the second-order boundary layer results present in Part I. Near the end of the asymptotic entry flow (Fig. 14b) large differences near the boundary layer edge are apparent. Near the surface the agreement is still quite good. In Part I the extent of validity of the second-order boundary layer theory is discussed in greater detail.

Finally, the shear parameter  $u_y$  is presented on Fig. 15 at various locations on the surface,  $y=-1$ . For very small values of  $\xi$ , the numerical solutions, the undisturbed

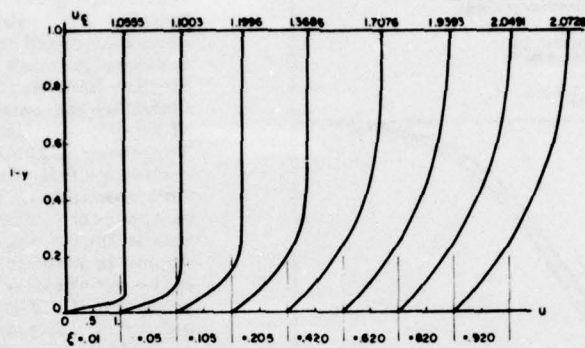


Fig. 12 Streamwise velocity profiles:  $z = 0.0$

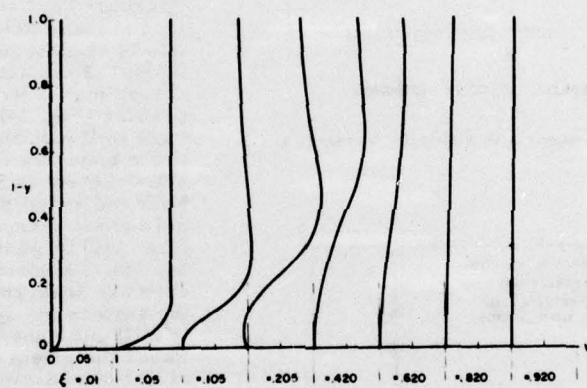


Fig. 13 Crossflow velocity profiles:  $z = -0.9$

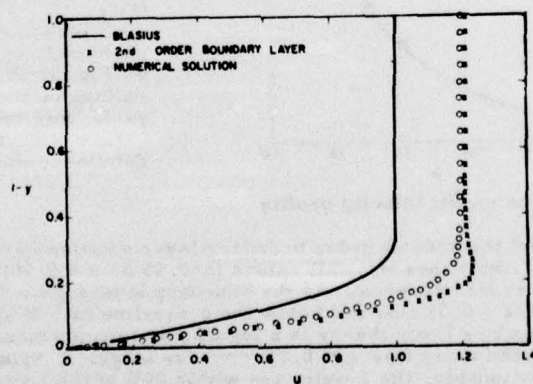


Fig. 14a Streamwise velocity profiles:  $\xi = 0.105, z = 0.0$

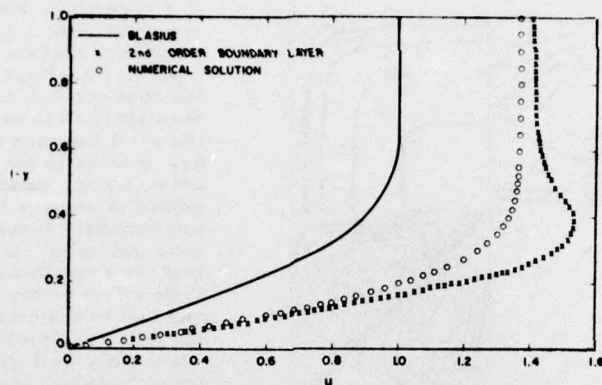


Fig. 14b Streamwise velocity Profile:  $\xi = 0.205$ ,  $z = 0.0$

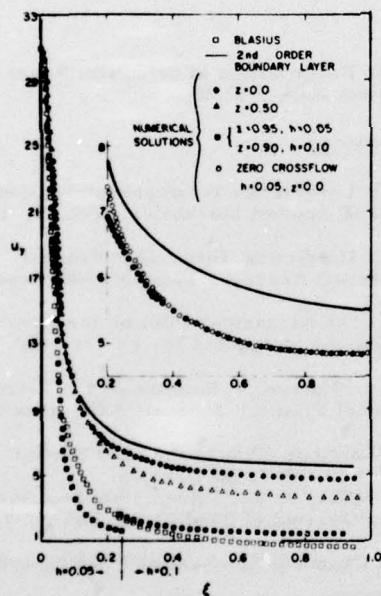


Fig. 15 Shear stress parameter:  $y = -1.0$

#### II. 4 Summary

Numerical solutions for the flow in a square channel have been obtained and agree reasonably well with the results of the entry region analysis of Part I. The numerical procedure is also applicable for rectangular ducts, and provides solutions for the axial and secondary motion that are fully converged at each axial location. The calculations are Reynolds number independent, so that for a given geometry only one set of results is required

motion are quite good. This reinforces our earlier conclusions that the axial flow is virtually insensitive to the secondary motion. On the other hand, the reverse is not true as the secondary motion near the walls changes significantly with mesh refinement, which has a much smaller effect on the axial flow behavior. Accurate secondary flow solutions near the walls would require much finer meshes. Since there is no available data for the secondary motion, finer mesh calculations were not considered. The solutions in the potential core, however, are reasonably accurate. Isovels and Isovors are given on Fig. 16. The predicted core velocity behavior  $u \sim 1+2\xi$  and  $v \sim -y$  is closely approximated. The constant vorticity lines clearly show the extent of the boundary layer growth.



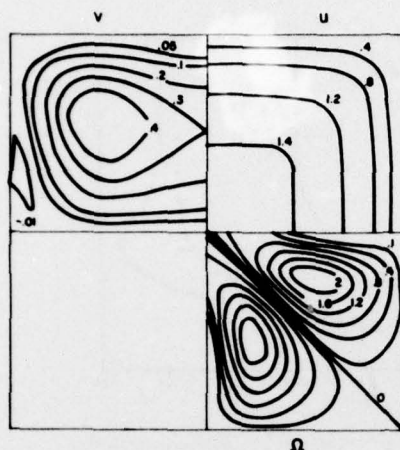


Fig. 16 Isovels and Isovors:  $\xi = 0.225$

for all Reynolds numbers. The secondary motion shows evidence of velocity reversal similar to that predicted by the entry analysis. Although the coarse mesh considered here appears to be adequate for the axial flow and the secondary motion in the potential core, a finer mesh is required to resolve the secondary boundary layer behavior near the walls. It is shown that the crossflows have little effect on the axial flow and that in the entry region, the latter is described reasonably well with second-order boundary layer theory.

This research was supported by the Air Force Office of Scientific Research under Grant No. AFOSR 74-2635, Project No. 9781-01.

#### REFERENCES

1. Han, L. S., "Hydrodynamic Entrance Lengths for Incompressible Laminar Flow in Rectangular Ducts," *Journal of Applied Mechanics*, Vol. 27, Trans. ASME, Vol. 82, 1960, pp. 403-409.
2. Briley, R., "A Numerical Method for Predicting Three-Dimensional Viscous Flows in Ducts," *United Aircraft Research Laboratories Report L110888-1*, 1972.
3. Carlson, G. A. and Hornbeck, R. W., "A Numerical Solution for Laminar Entrance Flow in a Square Duct," *Journal of Applied Mechanics*, Vol. 40, Trans. ASME, 1973, pp. 26-30.
4. Morihara, Hisoshi and Chang, R. A., "Numerical Solution of the Viscous Flow in the Entrance Region of Parallel Plates," *Journal of Computational Physics*, Vol. 11, 1973, pp. 550-572.
5. Wang, Y. L. and Longwell, P. A., "Laminar Flow in the Inlet Section of Parallel Plates," *AIChE Journal*, Vol. 10, 1964, pp. 323-329.
6. McDonald, J. W., Denny, V. E. and Mills, A. F., "Numerical Solution of the Navier-Stokes Equations in Inlet," *Journal of Applied Mechanics*, Vol. 39, Trans. ASME, 1972, pp. 873-878.
7. Van Dyke, Milton, "Entry Flow in a Channel," *Journal of Fluid Mechanics*, Vol. 44, Part 4, 1970, pp. 813-823.
8. Wilson, S. D. R., "Entry Flow in a Channel. Part 2," *Journal of Fluid Mechanics*, Vol. 46, Part 4, 1971, pp. 787-799.
9. Kapila, A. K., Ludford, G. S. S. and Olunloyo, V. O. S., "Entry Flow in a Channel. Part 3. Inlet in a Uniform Stream," *Journal of Fluid Mechanics*, Vol. 57, Part 4, 1973, pp. 769-784.
10. Rubin, S. G., "Incompressible Flow Along a Corner," *Journal of Fluid Mechanics*, Vol. 26, Part 1, 1966, pp. 97-110.
11. Rubin, S. G. and Grossman, B., "Viscous Flow Along a Corner: Numerical Solution of the Corner Layer Equations," *Quarterly of Applied Mathematics*, Vol. XXIX, 1971, pp. 169-186.

12. Saari, S., "Entry Flow in a Rectangular Channel, " Master of Science thesis (Aeronautics and Astronautics) Polytechnic Institute of Brooklyn, 1971.
13. Schlichting, H., Boundary Layer Theory, Sixth ed., McGraw-Hill Book Co., New York, 1968.
14. Lighthill, M. J., Introduction to Fourier Analysis and Generalized Functions, University Press, Cambridge, 1964. pp. 30-45.
15. Emmons, H. W. and Leigh, D. C., "Tabulation of the Blasius Function with Blowing and Suction," Aeronautical Research Council, London, Paper No. 157, 1953.
16. Rubin, S. G. and Lin, T. C., "A Numerical Method for Three-Dimensional Viscous Flow: Application to the Hypersonic Leading Edge," Journal of Computational Physics, Vol. 9, No. 2, 1972, pp. 339-364.
17. Forsythe, G. E. and Wasow, W. R., Finite Difference Methods for Partial Differential Equations, John Wiley & Sons, Inc., New York, 1960.
18. Carter, J. E., "Inverse Solution for Laminar Boundary-Layer Flows with Separation and Reattachment," NASA TR R-447, 1975.
19. Goldstein, R. J. and Kreid, D. K., "Measurement of Laminar Flow Development in a Square Duct Using a Laser-Doppler Flowmeter," Journal of Applied Mechanics, Vol. 34, Trans. ASME, Vol. 89, 1967, pp. 813-818.

reprinted from

Numerical/Laboratory Computer Methods in Fluid Mechanics

published by

THE AMERICAN SOCIETY OF MECHANICAL ENGINEERS

345 East 47th Street, New York, N.Y. 10017

Printed in U.S.A.



UNCLASSIFIED

SECURITY CLASSIFICATION OF THIS PAGE (When Data Entered)

Page 1

REPORT DOCUMENTATION PAGE		READ INSTRUCTIONS BEFORE COMPLETING FORM
1. REPORT NUMBER <b>AFOSR - TR - 77 - 0198</b>	2. GOVT ACCESSION NO.	3. RECIPIENT'S CATALOG NUMBER
4. TITLE (and Subtitle) <b>LAMINAR FLOW IN RECTANGULAR CHANNELS, PART I: ENTRY ANALYSIS, PART II: NUMERICAL SOLUTION FOR A SQUARE CHANNEL</b>		5. TYPE OF REPORT & PERIOD COVERED <b>INTERIM rept.</b>
6. PERFORMING ORG. REPORT NUMBER		7. CONTRACT OR GRANT NUMBER(s) <b>AFOSR 74-2635-74</b>
8. AUTHOR(s) <b>S. G. RUBIN, P. K. KHOSLA S. SAARI</b>		9. PROGRAM ELEMENT, PROJECT, TASK AREA & WORK UNIT NUMBERS <b>2307AT 61102F</b>
10. PERFORMING ORGANIZATION NAME AND ADDRESS <b>POLYTECHNIC INSTITUTE OF NEW YORK AERODYNAMIC LABORATORIES/ ROTE 110 FARMINGDALE, N Y 11735</b>		11. REPORT DATE <b>Dec 76</b>
12. CONTROLLING OFFICE NAME AND ADDRESS <b>AIR FORCE OFFICE OF SCIENTIFIC RESEARCH/NA BLDG 410 BOLLING AIR FORCE BASE, D C 20332</b>		13. NUMBER OF PAGES <b>23</b>
14. MONITORING AGENCY NAME & ADDRESS (if different from Controlling Office)		15. SECURITY CLASS. (of this report) <b>UNCLASSIFIED</b>
16. DISTRIBUTION STATEMENT (of this Report)  <b>Approved for public release; distribution unlimited.</b>		15a. DECLASSIFICATION/DOWNGRADING SCHEDULE
17. DISTRIBUTION STATEMENT (of the abstract entered in Block 20, if different from Report)  <b>410 012</b>		
18. SUPPLEMENTARY NOTES  <b>Proceedings of the ASME Symposium on Numerical/Laboratory Computer Methods in Fluid Mechanics pp29-51 Dec 76</b>		
19. KEY WORDS (Continue on reverse side if necessary and identify by block number) <b>RECTANGULAR CHANNELS SECONDARY FLOW MASS INJECTION ASYMPTOTIC ANALYSIS REYNOLDS NUMBER INDEPENDENCE</b>		
20. ABSTRACT (Continue on reverse side if necessary and identify by block number) <b>Laminar incompressible flow in rectangular channels is considered. In Part I, the entry region is evaluated by a boundary layer/potential core analysis. It is shown that the three-dimensional displacement induced potential flow can be described with a pair of two-dimensional potential functions. Second-order boundary layer solutions, with and without surface mass transfer, are determined, an interesting secondary flow reversal is predicted. In Part II, numerical solutions are obtained for the viscous channel equations, which are derived from the asymptotic theory of Part I. A two stream function, velocity, vorticity</b>		

DD FORM 1 JAN 73 1473 EDITION OF 1 NOV 65 IS OBSOLETE

UNCLASSIFIED

SECURITY CLASSIFICATION OF THIS PAGE (When Data Entered)

UNCLASSIFIED

SECURITY CLASSIFICATION OF THIS PAGE(When Data Entered)

system, independent of the Reynolds number, is solved with a combined iterative ADI/point-relaxation numerical procedure. A single calculation applies for all Reynolds numbers, which appears only in the coordinate scaling. The axial flow behavior of Parts I and II are in good agreement in the asymptotic entry region where both analyses apply. Secondary flow reversal is calculated; however, the grid is too crude for quantitative comparisons. Numerical solutions are obtained until fully developed conditions are achieved. Agreement with experimental data is good.

UNCLASSIFIED

SECURITY CLASSIFICATION OF THIS PAGE(When Data Entered)